JOURNAL OF GEOPHYSICAL RESEARCH, VOL. 104, NO. C5, PAGES 11,515–11,527, MAY 15, 1999

Sea ice extent mapping using Ku band scatterometer data

Quinn P. Remund and David G. Long

Department of Electrical and Computer Engineering, Brigham Young University, Provo, Utah

Abstract. Although spaceborne scatterometers such as the NASA scatterometer have inherently low spatial resolution, resolution enhancement techniques can be used to increase the utility of scatterometer data in monitoring sea-ice extent in the polar regions, a key parameter in the global climate. The resolution enhancement algorithm produces images of A and B, where A is the normalized radar backscatter coefficient σ^o at 40° incidence and B is the incidence angle dependence of σ^o. Dual-polarization A and B parameters are used to identify sea ice and ocean pixels in composite images. The A copolarization ratio and vertically polarized B are used as primary classification parameters to discriminate between sea ice and open ocean. Estimates of the sea-ice extent are obtained using linear and quadratic (Mahalanobis distance) discriminant boundaries. The distribution parameters needed for the quadratic estimate are taken from the linear estimate. The σ^o error variance is used to reduce errors in the linear and Mahalanobis ice/ocean classifications. Noise reduction is performed through binary image region growing and erosion/dilation techniques. The resulting edge closely matches the NASA Team algorithm special sensor microwave imager derived 30% ice concentration edge. A 9-month data set of global sea-ice extent maps is produced with one 6-day average map every 3 days.

1. Introduction

Several factors motivate the interest in monitoring the extent of sea ice. Sea-ice extent is a critical input to global climate and geophysical models. Polar ice sheets act as insulating layers between the relatively warm ocean and cool atmosphere and can radically change the albedo of the Earth's surface. It also plays a vital role in the planetary water exchange cycle. Moreover, sea-ice extent may be used as a sensitive indicator of global climate change [*Budd*, 1975]. Hence monitoring the extent of sea ice is of great interest to the remote sensing community.

In addition to climatological reasons, sea-ice mapping is needed for retrieval of ocean wind velocities from scatterometer measurements. The NASA scatterometer (NSCAT) was designed to infer surface wind speed and direction over the ocean. If measurements are included that are corrupted by nonocean surfaces such as sea ice, the wind estimates are degraded. Thus accurate knowledge of the location of sea ice is required. In this paper, an adaptive technique for mapping the sea-ice extent using NSCAT data is developed and compared to special sensor microwave imager (SSM/I) derived ice maps. Using the methods discussed in this paper, 6-day average ice extent maps are processed every 3 days over the 9 months of NSCAT data. The ice maps are used in the final reprocessing of the NSCAT data.

Historically, spaceborne scatterometers have been employed primarily in atmospheric and oceanic studies. Rapid repeat coverage makes these instruments valuable in these applications. The low spatial resolution of scatterometers is suitable for studying such large-scale phenomena. Spaceborne scatterometers have also been used to study nonocean surface parameters [*Long and Drinkwater*, 1994, *Hosseinmostafa et al*., 1995]. However, for land and ice studies, the low resolution can limit the utility of this data.

The scatterometer image reconstruction with filter (SIRF) algorithm was developed to enhance scatterometer image resolution by combining data from multiple passes of the satellite [*Long et al*., 1993]. It uses multiple σ^o values to increase the effective resolution of the data. Over a limited incidence angle range of [20°, 55°], σ^o (in decibels) is approximately a linear function of θ,

$$\sigma^o(\theta) = A + B(\theta - 40°) \tag{1}$$

where A and B are functions of surface characteristics, azimuth angle, and polarization. A is the σ^o value at 40° incidence and B describes the dependence of σ^o on θ. A and B provide valuable information about surface parameters. Forty degrees is chosen as a midswath value, but any interior swath angle can be used. The SIRF algorithm produces both A and B images from NSCAT σ^o measurements.

This paper describes the development and implementation of an adaptive sea-ice extent mapping method and its comparison to SSM/I derived maps. Section 2 describes the resolution-enhanced parameters used in the multivariate analysis of the data. Section 3 gives an overview of the sea-ice mapping technique and discusses each of the steps in detail. The technique is applied to NSCAT polar data and the results are given in section 4. The final section contains the conclusions drawn from the analysis.

2. Polar NSCAT Data

The NASA scatterometer, launched in August 1996, is a real-aperture, dual-polarization Ku band radar scatterometer designed to measure the normalized radar backscatter coefficient σ^o of the Earth's surface. Using the SIRF algorithm, dual-polarization A and B images with an effective resolution of 8–10 km can be generated with 6 days of data. NSCAT

Copyright 1999 by the American Geophysical Union.

Paper number 98JC02373.
0148-0227/99/98JC-02373$09.00

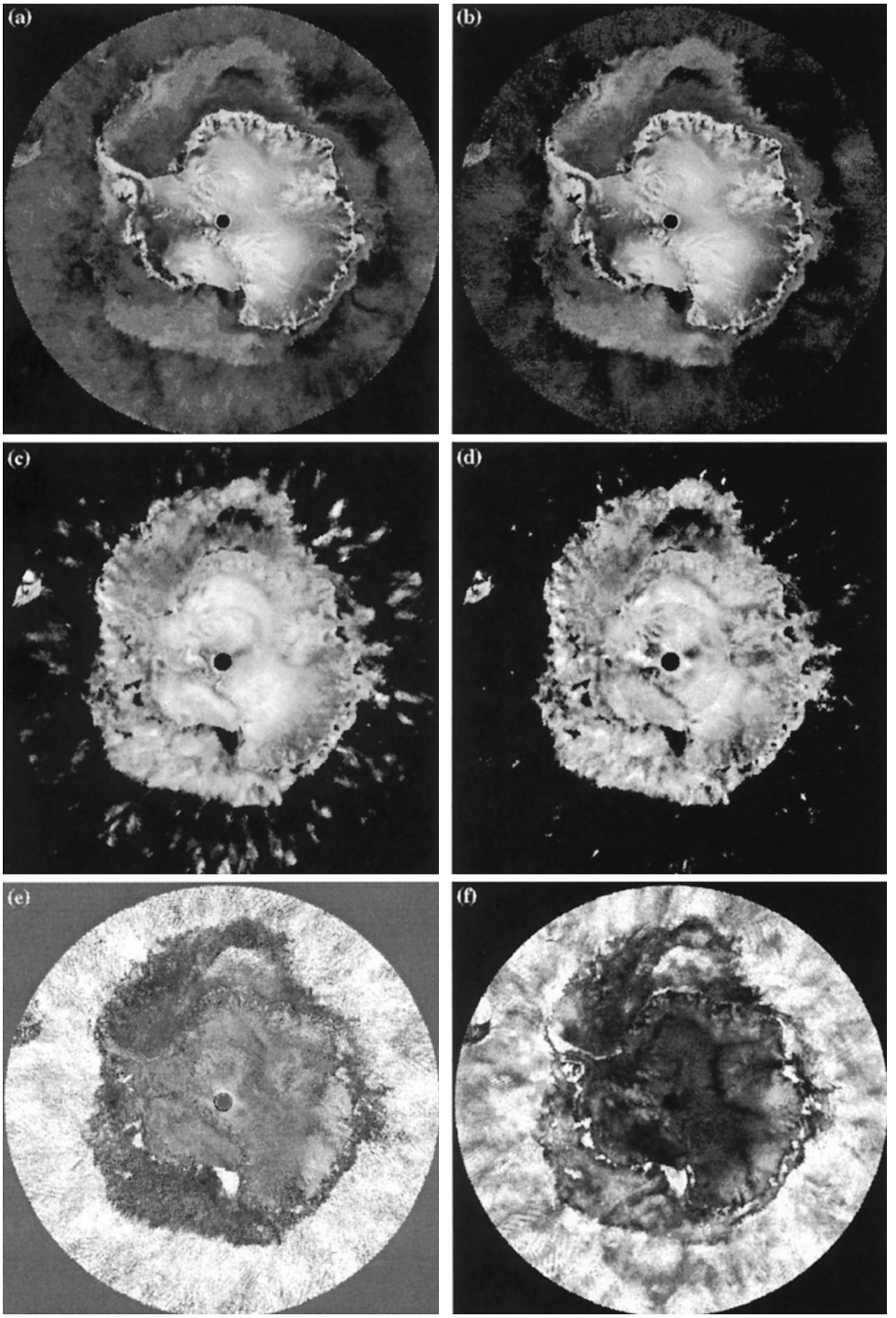

Figure 1. Scatterometer image reconstruction with filter (SIRF) enhanced resolution NASA scatterometer (NSCAT) Antarctic images for the day range 1996 Julian Day (JD) 337–342, showing (a) v pol σ^o at 40° incidence (A_v), (b) h pol σ^o at 40° incidence A_h, (c) v pol incidence angle dependence of σ^o B_v, (d) h pol incidence angle dependence of σ^o B_h, (e) copol ratio γ, and (f) σ^o error standard deviation κ.

vertical polarization (v pol) images can be produced with only 3 days of data since there are more v pol antenna beams than horizontal polarization (h pol) beams. However, 6 days are used to ensure that the h pol data provide enough coverage to create the reconstructed image. Since the v pol images are reconstructed with more measurements, the qualities of the A and B estimates are subjectively superior to the h pol images. We recognize that sea-ice dynamics may cause the ice edge to change significantly during a 6-day interval. As a result, the ice maps generated by this technique must be regarded as average ice extents during the imaging period. The method can be applied with data over shorter intervals (especially in the Arctic region), with some loss of coverage and degradation of the h pol image quality.

The dual-polarization A and B values for each pixel provide four parameters that can be used to detect sea ice. In addition,

σ^o error standard deviation is also useful. These parameters are described in the remainder of this section. Their utility in the discrimination between sea ice and open ocean is also discussed.

2.1. Copolarization Ratio

A useful parameter in the discrimination of sea ice and ocean is the copolarization (copol) ratio, defined as the ratio of σ^o_{vv} and σ^o_{hh} [*Yueh et al*., 1997]. This can be extended to a copol ratio of the incidence angle normalized σ^o values. For the purposes of this paper, the copol ratio γ is defined as the ratio of the A_v and A_h values:

$$\gamma = A_v/A_h. \tag{2}$$

In log space this is equivalent to taking the difference between the v and h components. Sample A_v and A_h images are shown in Figures 1a and 1b. The corresponding γ image is shown in Figure 1e.

The copol ratio is sensitive to the surface-scattering mechanisms. For smooth, conductive surfaces such as calm seawater, the reflection coefficients for vertically and horizontally polarized incident waves differ. In general, vertically polarized waves reflect more than their horizontal counterparts. Thus the copol ratio (in decibels) is positive. For rough surface dielectric layers with randomly oriented scatterers such as ice or snow, multiple reflections of the incident radiation tend to depolarize it. As a result, vertical and horizontal waves are scattered similarly and the copol ratio is closer to 0 dB. Further, the copol ratio is sensitive to the presence of ice or water even in single (Bragg) scattering situations. In these scenarios the polarization ratio is determined by the relative permittivity of the material. Since sea ice has a much lower permittivity than ocean water, γ is also much lower. Because of these differences in scattering mechanisms, γ is useful in discriminating between different ice and ocean surfaces. While the ocean generally has high γ values and sea ice (with low water content) generally has low values, in high wind conditions some ocean areas may exhibit low copol ratios. The winds induce roughness on the ocean surface, which depolarizes the scattering and drives γ down. In order to overcome this, other parameters are used to assist in the classification.

2.2. Incidence Angle Dependence

The incidence angle dependence of σ^o, represented by B, is also sensitive to the presence of sea ice [*Drinkwater*, 1998; *Rouse*, 1969; *Gohin and Cavanie*, 1994; *Gohin*, 1995]. Figures 1c and 1d give examples of B_v and B_h enhanced resolution images, respectively. Owing to the increased scattering isotropy of sea ice [*Early and Long*, 1997] relative to the ocean, these regions tend to have less incidence angle dependence. On the other hand, ocean σ^o measurements are strongly dependent on incidence angle, with the low incidence angles exhibiting higher σ^o. Thus this parameter can be used to limited degrees of accuracy in differentiating between the ice and ocean. While it may be useful to use both B_v and B_h, this study found a strong correlation between B_v and B_h. Noting that B_v values are less noisy than B_h owing to the greater number of vertical polarization measurements, only B_v is used for the discriminant analysis.

2.3. The σ^o Estimate Error Standard Deviation

In addition to the copol ratio and incidence angle dependence, the standard deviation of the error in the σ^o estimates also contains information about polar surfaces. This metric, denoted κ, is a measure of the amount of surface response change over the ensemble of σ^o measurements due to temporal or azimuthal variability.

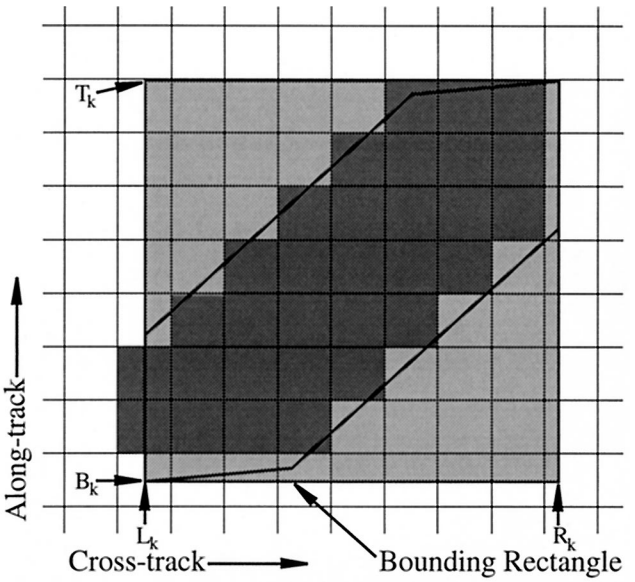

Figure 2. An integrated NSCAT σ^o cell overlaying the high-resolution grid. Only the shaded square grid elements have nonzero values of the resolution element weighting function $h(x, y)$. The bounding rectangle is also indicated. Figure is adapted from *Long et al.* [1993] (@ 1993 IEEE).

In order to understand κ, we examine the measurement collection process and its relation to image reconstruction. For NSCAT, each fan beam antenna illumination pattern is resolved in the along-beam direction through Doppler filtering along iso-Doppler lines in the footprint [*Naderi et al*., 1991]. The beam is resolved into 25 cells at different incidence angles. The size of each cell depends upon its relative location in the beam with near-nadir cells covering a smaller area on the surface. The cells have a hexagonal shape determined by the Doppler filtering, motion of the satellite, and azimuth beamwidth of the antenna [*Naderi et al*., 1991].

Figure 2 shows an example NSCAT cell overlaid on a SIRF resolution grid. SIRF produces A and B estimates for each resolution element. The forward projection of the A and B values yields an estimate for σ^o given by

$$\hat{\sigma}^o = \frac{1}{N} \sum_{i=L_k}^{R_k} \sum_{j=B_k}^{T_k} h_k(i, j)[A(i, j) + B(i, j)(\theta - 40°)] \tag{3}$$

where N is the number of pixels in the cell; L_k, R_k, T_k, and B_k define a bounding rectangle for the kth hexagonal σ^o measurement cell; $h_k(i, j)$ is the weighting function for the (i, j)th resolution element (for NSCAT a simplified weighting can be used),

$$h_k(i, j) = \begin{cases} 1 & \text{pixel in } k\text{th cell} \\ 0 & \text{otherwise} \end{cases} \tag{4}$$

$A(i, j)$ is the A estimate for the (i, j)th resolution element, and $B(i, j)$ is the B estimate for that pixel (see Figure 2). For each NSCAT σ^o measurement, we compute the associated forward projection $\hat{\sigma}^o$. The difference between the measured and forward projected σ^o, $(\sigma^o - \hat{\sigma}^o)$ for each pixel is computed. The parameter κ is defined as the standard deviation of

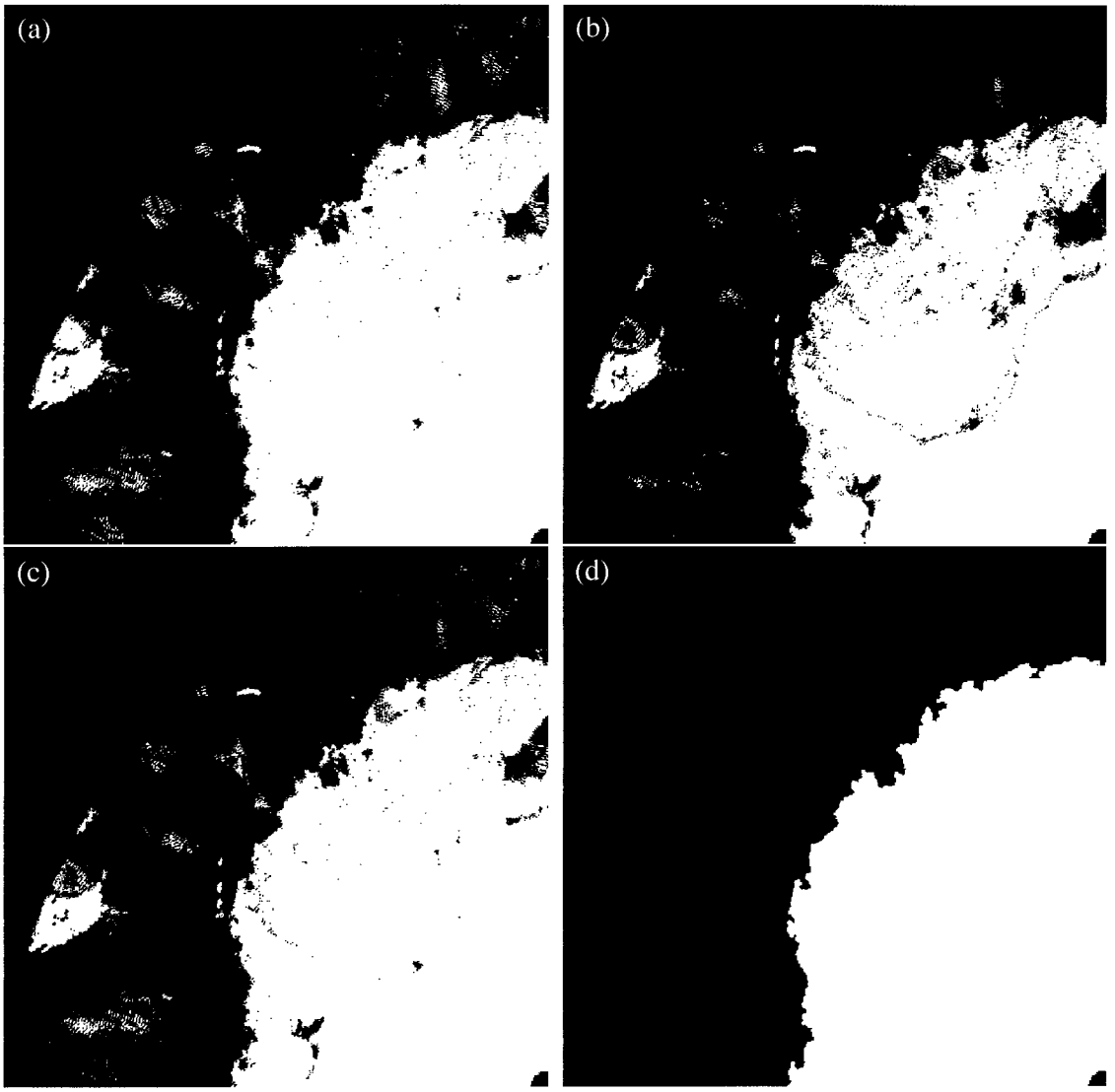

Figure 3. Binary images at different stages of the ice/ocean discrimination process for a single quadrant of the Antarctic 1996 Julian Day (JD) 337–342 image. The images are the (a) linear discriminant estimate, (b) Mahalanobis distance estimate, (c) with κ correction applied, and (d) the result of the erosion, region-growing, and dilation procedures.

the measurements in the ensemble of this random variable for each pixel:

$$\kappa = \sqrt{\sum_{l} (\sigma_l^o - \hat{\sigma}_l^o)^2} \tag{5}$$

where the σ_l^o are the vertical polarization measurements touching the pixel. While this study used the SIRF A and B estimates to compute κ, estimates obtained from linear regression and simple binning may also be used, although the resulting κ images would have lower spatial resolution.

Figure 1f illustrates an example κ image. Ideally, the standard deviation κ would be zero if SIRF perfectly reconstructed the measurements into the A and B images. However, temporal change of the surface, noise in the σ^o measurements, and azimuthal anisotropy of σ^o may cause κ to increase, though, unfortunately, the time and azimuth components are inseparable in this metric. The ocean response tends to be very dynamic in both time and azimuth owing to varying wind-induced surface roughness, resulting in large κ values. Although higher κ values are expected in ocean regions than for sea ice, consistently calm ocean areas during the data collection period may produce low κ values. Sea-ice response, on the other hand, is less time dependent, although ice melt/freeze events or ice motion may cause some variance. Azimuthal anisotropy in sea-ice regions is generally less than 1 dB for C band ERS 1 data [*Early and Long*, 1997]. Albeit in a different year and season, a duplicate study was performed for NSCAT data and showed that the anisotropy was less than 0.6 dB in the same study regions [*Remund et al.*, 1997]. We recognize that sea-ice conditions may be different in these study regions owing to the different data time frames. Regardless, we expect that azimuthal variability is lower for sea ice than open ocean.

3. Sea-Ice Extent Mapping Technique

The parameters discussed in section 2 provide the information needed to map sea-ice extent in the polar regions.

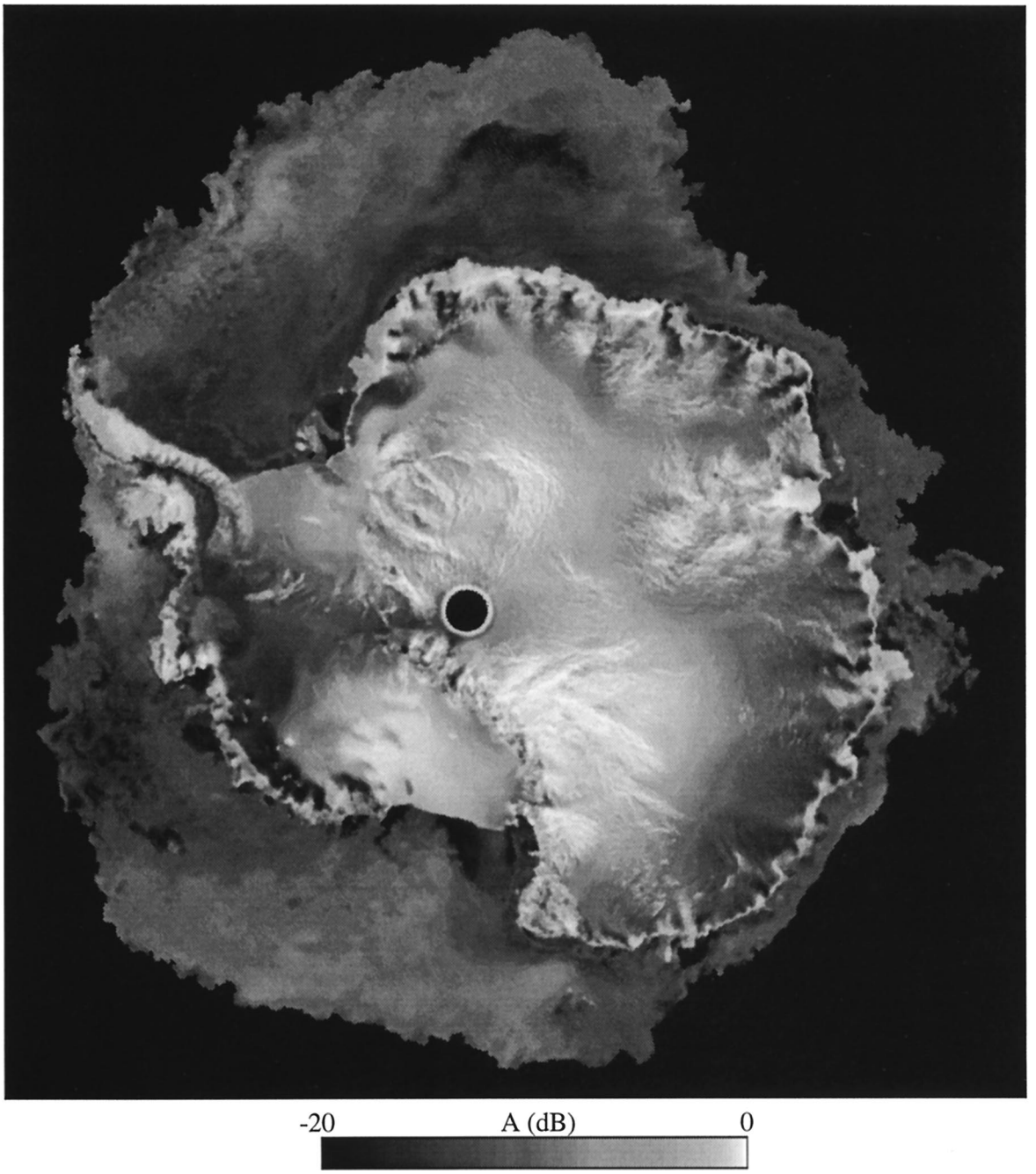

Figure 4. Antarctic ice-masked image using the NSCAT technique for 1996 JD 337–342.

Through proper processing, the presence or absence of sea ice can be inferred from the γ, B_v, and κ images. This section discusses a technique for generating polar ice extent maps from these parameters. First, an overall strategy is described by enumerating the individual steps. Next, a description and analysis of each step is presented.

3.1. Technique Overview

Several steps are combined to define an ice extent mapping technique that adaptively handles the time variant parameter distributions. The technique can be summarized as follows: (1) Produce the enhanced resolution γ, B_v, and κ images. (2) Generate γ versus B_v bivariate distribution of the images. (3) Perform linear discrimination (LD) to obtain a first estimate of the sea-ice extent, finding the optimal linear discrimination boundary and performing pixel by pixel classification. (4) Compute the means, variances, and covariances of the ice and ocean regions for both parameters. (5) Perform the Mahalanobis distance (MD) discrimination, finding the Mahalanobis quadratic discrimination boundary and performing pixel by pixel classification. (6) Apply the κ correction by thresholding κ at 3.3 for all pixels for which the LD and MD estimates differ. (7) Perform edge filtering to reduce noise, so region growing removes isolated noise patches and erosion/dilation techniques low-pass filter the edge.

Illustrative examples of the binary output images at different

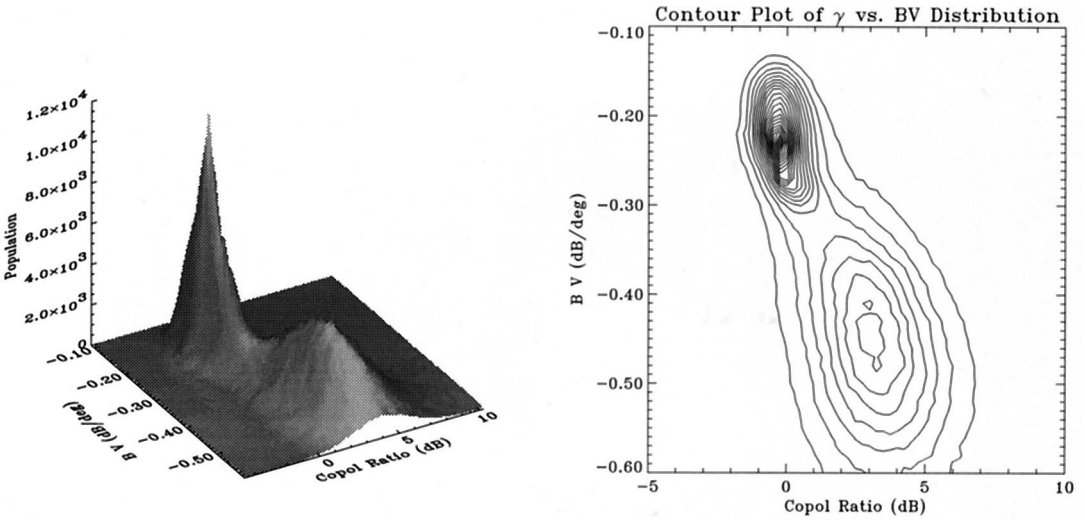

Figure 5. (left) Two-dimensional distribution of copolarization (copol) γ versus B_v values and (right) its corresponding contour plot for NSCAT data from 1996 JD 337–342. The two modes represent ice and ocean pixels. Each mode clearly has different mean and variance values. The upper left mode is sea ice, while the other represents ocean pixels.

stages of the detection technique are shown in Figure 3 for one quadrant of the Antarctic image. Figure 4 illustrates an A_v image masked by the ice extent estimate generated by our method.

3.2. Multiparameter Discrimination

The three parameters γ, B_v, and κ contain varying degrees of information about the surface response that can be used to differentiate between sea-ice and open ocean pixels in the images. Of the three parameters, γ and B_v are the most sensitive to sea-ice presence. This can be seen in the example images in Figure 1. The κ image has the most ambiguity in differentiating between the different surfaces. Indeed, when a simple threshold discrimination is implemented with each parameter individually, κ has the weakest performance. For this reason, γ and B_v are used as the primary discrimination parameters. However, the κ images can be used to reduce residual errors in localized regions when the other two are used. This will be shown in section 3.3.

The two-dimensional distribution of nonland pixels for the two primary parameters contains two distinct modes that correspond separately with sea-ice and ocean pixels. An example is shown in Figure 5 with its corresponding contour plot. Through the proper choice of a discriminant boundary, the modes can be separated to obtain an ice extent estimate. Owing to the seasonal variations in ice extent and scattering characteristics, the distribution is season dependent. Thus the optimal mode-separating boundary must adapt to the specific distribution for each 6-day imaging period.

Two major steps are used in the sea-ice extent mapping technique: linear discrimination and Mahalanobis distance discrimination. The first uses a linear boundary to separate the modes of the bivariate data, while the second uses a quadratic boundary.

3.2.1. Linear discrimination. If the underlying ice and ocean component distributions of the joint distribution are Gaussian, the optimum linear discriminant boundary passes through the saddle point of the distribution function and is perpendicular to the line passing through the peaks of the two modes. This line can be found in an automated fashion. First, the mode peaks are located by a 5×5 bin search of the bivariate distribution. These are found by starting two separate searches in regions of the γ-B_v plane known to be in the different modes of the distribution. The search procedure ascends to each local peak. A 5×5 window is used to ensure that the search does not get hung on any local maxima. The saddle point is then located along the line connecting the two peaks of the distribution at the bin with the minimum value along the line. The linear discriminant boundary is computed as the line passing through the saddle point and perpendicular to the peak-to-peak line.

Using the linear boundary, each pixel is classified as ice or ocean by observing its associated parameter values. Pixels on one side of the line are considered ice, while the others are classified as ocean. Figure 6 shows the γ versus B_v distribution contour plots of images from four different NSCAT time frames. The linear discriminant boundary is also plotted. Note that as the distribution characteristics change with season, the technique adaptively assigns an optimum decision boundary. The result of the linear discrimination is a binary image of ice and ocean locations.

Once an ice extent estimate image is produced, the means, variances, and covariances are computed for the ice pixels and the ocean pixels. These are used as statistical estimates for the Mahalanobis distance classification.

3.2.2. Mahalanobis distance discrimination. The Mahalanobis distance aids in separating the modes of a multimodal distribution where each component distribution is Gaussian with different variances [*Duda and Hart*, 1973]. It accounts for the variance differences through the use of a quadratic rather than a linear boundary. The squared Mahalanobis distance is given by

$$r^2 = (\mathbf{x} - \boldsymbol{\mu})^T \Sigma^{-1} (\mathbf{x} - \boldsymbol{\mu}) \tag{6}$$

where $\mathbf{x}$ is the vector of parameters for the test pixel, $\boldsymbol{\mu}$ is the reference vector containing the component distribution means, and Σ is the covariance matrix.

Subjectively noting that the underlying component distribu-

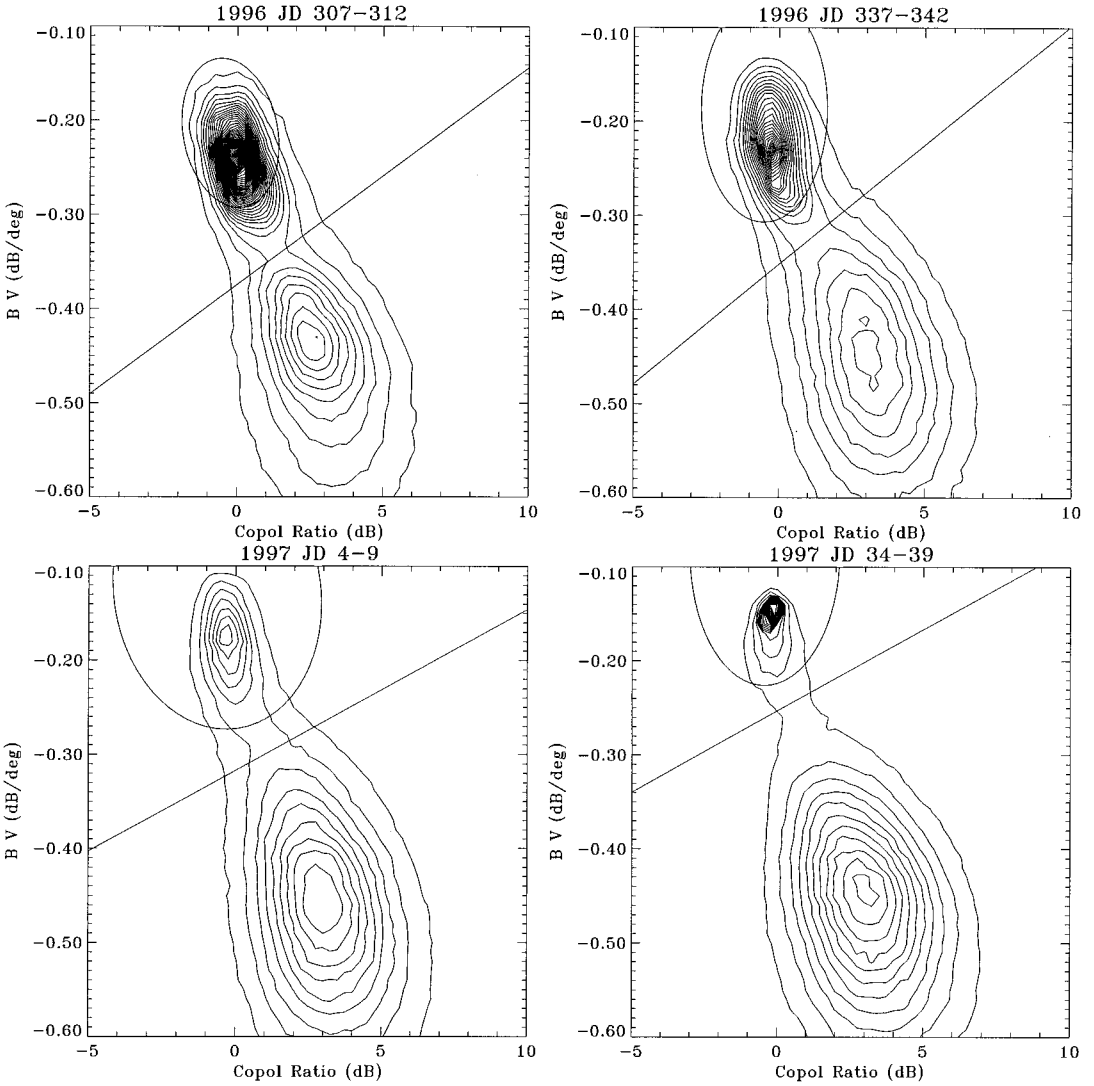

Figure 6. Contour plots of four γ versus B_v distributions. The Mahalanobis and linear discriminant boundaries are also plotted. The decision boundaries are adapted to be optimum for each individual distribution.

tions of the bivariate γ-B_v distribution appear nearly Gaussian, the Mahalanobis distance can be applied in the discrimination of sea ice and ocean pixels. For each pixel of interest, two Mahalanobis distances are computed, r_{ice} and r_{ocean}. If r_{ice} is less than r_{ocean}, the pixel is flagged as ice; otherwise, the pixel is considered ocean. Figure 6 shows the distribution contours plotted with the Mahalanobis and the linear discriminant boundaries. Clearly, the boundaries adapt for the particular characteristics of a given imaging period distribution.

3.3. The κ Correction

The linear discriminant and Mahalanobis distance binary ice extent images both provide visually good estimates of the ice extent. In general, the same ice edges are observed in the LD and MD estimates, with the exception of relatively small localized errors. Local errors in the LD estimates tend to overestimate the ice edge. On the other hand, the MD edges usually do not show these overestimation errors but have some localized regions where the ice edge is underestimated. As described previously, consistently high winds during the data collection period may drive γ down, resulting in false ice detection when the LD method is applied. The same weather mechanism that causes this error also increases κ since high winds over the time frame of the data collection induce higher azimuthal anisotropy and temporal variance of σ^o. The overestimation error regions of the LD images have characteristically high κ values. The correlation between LD errors and high κ suggests that κ can be used as a secondary discrimination parameter to correct for errors in the LD and MD images.

The κ correction is applied to the set of all pixels for which the LD and MD images disagree. Thus κ becomes the deciding factor when LD and MD yield different discrimination outputs. The set consists of all LD overestimation pixels and all MD underestimation pixels. An empirical analysis of the κ data over this set of pixels for several sample images showed that κ is generally above 3.3 for the LD error pixels. The correction is then applied by thresholding κ over the error set using the following discrimination rule:

$$\text{pixel}_{ij} = \begin{cases} \text{ice} & \kappa_{i,j} < 3.3 \\ \text{ocean} & \kappa_{ij} \geq 3.3 \end{cases} \tag{7}$$

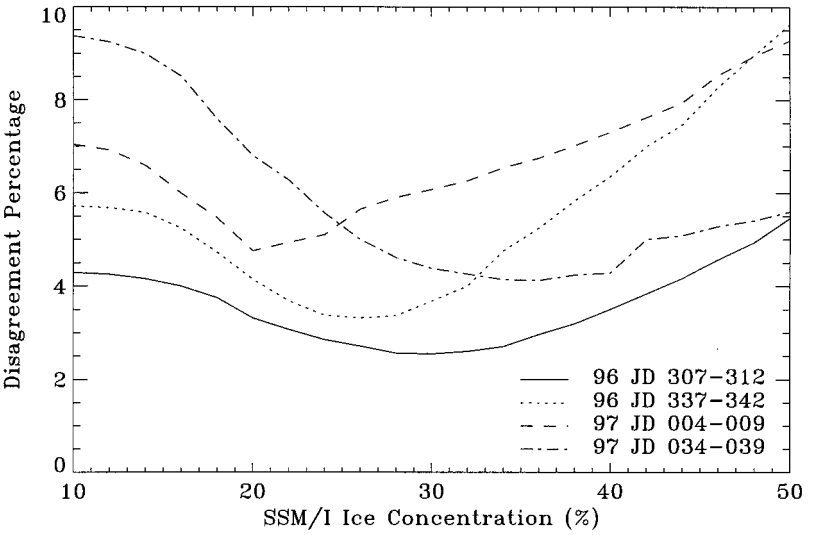

Figure 7. Percentage of the sea-ice area that the NSCAT and special sensor microwave image (SSM/I) ice extent maps disagree as a function of SSM/I ice concentration. This metric is computed by finding the ratio of the area for which the two methods disagree to the area classified as ice for either method. Four sample NSCAT images were used. The minimum generally occurs very close to 30%.

where $\kappa_{i,j}$ is κ for the i, jth pixel in the set of pixels for which LD and MD disagree.

3.4. Ice Map Filtering

The κ correction results in a binary image illustrating the location of sea-ice and ocean regions. However, some residual high-wind-induced noise over the ocean can cause ocean pixels to be misclassified as ice for reasons previously addressed. This noise is manifested in the binary image as patches of ocean that have been classified as sea ice. Other physical mechanisms may also cause patches of ice to be misclassified as ocean. The former is much more common than the latter. These anomalies often occur in isolated regions disconnected from the actual edge but may also occur on the edge itself. Each of these is handled separately in the filtering step.

Region growing techniques are used to eliminate the isolated misclassification patches in the ocean and ice. The region growing method starts with a small region known to be within the ice area (the land mass for the Antarctic region). It then expands this region within the ice area of the binary ice mask image. The region continues to grow until it gets to the outer edge of the ice region and cannot expand further. This eliminates all the isolated patches of pixels misclassified as ice in the ocean. The region growing method is then inverted to grow from the outer edge of the image inward until it reaches the binary threshold edge. This eliminates all the patches of pixels misclassified as ocean in the ice.

Once the region growing is complete, some residual noise exists on the edge itself as high spatial frequency edge characteristics and as small lobes attached by only a few pixels to the main body of ice. To remove these, image erosion and dilation techniques are used [*Rush*, 1995]. Two erosion iterations separate the smaller misclassified lobes from the main body. Region growing is then performed again to eliminate these separated lobes. To restore the edge (a low-pass-filtered version), two iterations of image dilation are performed. We recognize that small fingers of ice extending from the main ice pack may be filtered out along with the edge noise. The result is a binary image mask that can be applied to the original A or B images (see Figure 3).

The filtering operation is designed to map the sea-ice extent rather than absolute sea-ice coverage. Consequently, open water regions within the ice pack are filtered out by the inverse region growing step. The filtering can be modified to preserve these regions by eliminating the inverse region growing step.

4. Results

The technique is implemented for all data during the NSCAT mission. Each enhanced resolution image is constructed using 6 days of data with 3 days of overlap in consecutive time frames. The result is a long time series of sea-ice extent images that can be used in a variety of applications including the ice masking needed in wind retrieval reprocessing of NSCAT data. In this section, the NSCAT and NASA Team algorithm SSM/I derived ice maps are compared and the seasonal ice extent as generated by both methods is observed.

4.1. Comparison With NASA Team Algorithm SSM/I Derived Ice Maps

Because of the limited amount of high-resolution data during the NSCAT mission, validation is difficult. To provide validation for our technique, the NSCAT ice maps are compared with SSM/I derived ice concentration images. This product is derived from passive multifrequency, dual-polarization special sensor microwave imager observations using the NASA Team algorithm [*Cavalieri et al.*, 1991, 1984]. The NSCAT images use a polar stereographic projection similar to the projection used for the SSM/I images but are produced at a higher pixel resolution. Daily SSM/I ice concentration images were obtained from the National Snow and Ice Data Center (NSIDC). For each NSCAT image the corresponding six SSM/I images were averaged together. For comparison with NSCAT results, the SSM/I average ice concentration image for the same time period is thresholded at the desired concentration level to create a binary ice map. This image is then inter-

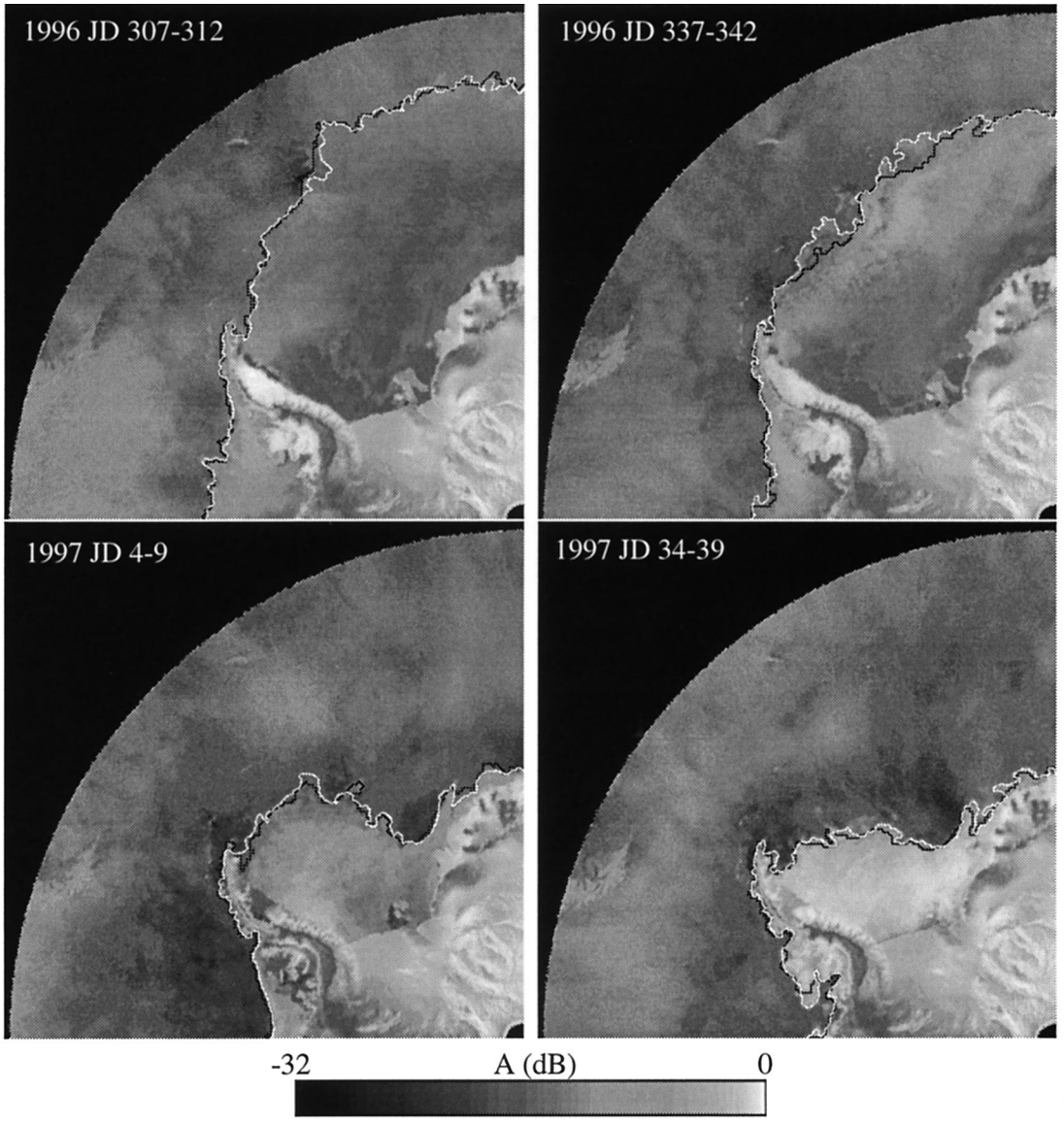

Figure 8. NSCAT scatterometer image reconstruction with filter (SIRF) resolution enhanced A_v images of a portion of Antarctica. The NSCAT ice edge is plotted in white. The NASA Team algorithm SSM/I derived 30% ice concentration edge is plotted in black.

polated to the NSCAT pixel resolution by determining which NSCAT pixels correspond to each SSM/I pixel and filling them with the associated SSM/I pixel value.

Four sample time periods were used for the validation. The images are each spaced by approximately 1 month to illustrate the changes in sea-ice extent throughout the yearly melt cycle. The resulting ice extent maps are compared with various NASA Team algorithm ice concentration images thresholded at various levels from 10% to 50%. To provide a quantitative measure of correlation between the two ice maps, the disagreement percentage is used. While this is not an ideal metric, it is easily defined as the ratio of the area of the pixels where the NSCAT and the NASA Team methods disagree and the area of the pixels that are classified as ice by either method. Figure 7 shows this metric as a function of NASA Team algorithm ice concentration for the four sample images. In most cases the minimum occurs at approximately 30%. We conclude that the NSCAT ice edge corresponds most closely with a 30% ice concentration.

Figure 8 shows several sample SIRF A_v images for a quadrant of Antarctica with the associated NSCAT and NASA Team 30% ice edge estimates. These images consist of the quadrant of Antarctica from 90° west longitude (lower edges of the images) to 0° longitude (right edges of the images). Subjectively, there is a high correlation between the edges. For the images with time periods 1996 Julian day (JD) 307–312 and 337–342 and 1997 4–9 and 34–39, the disagreement percentages are 2.19%, 3.24%, 5.47%, and 3.56%, respectively. Some of the disagreement is due to the differences in image resolutions and pixel spacing since the enhanced resolution NSCAT images have higher spatial resolution than the SSM/I images.

The disagreement percentage metric is also calculated for every image in the NSCAT data set using the corresponding NASA Team 30% ice concentration images and is shown in

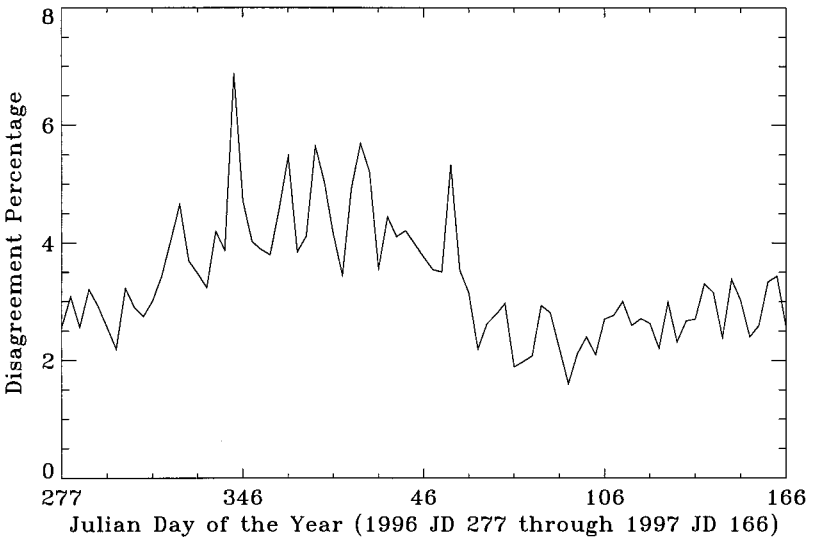

Figure 9. Plot of disagreement percentage metric computed by taking the ratio of surface area where the two methods disagree and the area for which either method classifies the surface as sea ice. The images each represent 6 days of data with 3 days of overlap between consecutive images. The Julian days given on the horizontal axis correspond to the first days of each imaging period.

Figure 9. The set consists of 80 images spanning the time period from 1996 JD 277–282 to 1997 JD 166–171. For the most part the disagreement percentage is between 2% and 5%. The mean value is 3.34%, and the standard deviation is 1.01%. The correlation between the NSCAT and NASA Team ice-mapping techniques is strong throughout the NSCAT mission period.

The time period when the disagreement percentage is the greatest is during the ice retreat phase. During this time the NSCAT estimated ice extent is generally greater than the SSM/I ice extent. Figure 8 (top right) illustrates this effect. The NSCAT edge identifies a portion of the ice pack that the SSM/I does not. *Fetterer et al.* [1992] observed a similar trend in comparing NASA Team and Geosat radar altimeter ice edges.

4.2. Seasonal Sea Ice Extent

We now consider the seasonal area of the sea-ice extent as computed from the NSCAT and NASA Team ice maps. The sea-ice extent area for a particular image is computed by finding the area for each ice-flagged pixel according to the polar stereographic projection. These areas are summed to obtain the total extent. It should be noted that this is the total ice extent rather than the total ice area since polynyas are not masked out in the images. Figure 10 shows the seasonal ice extent computed for the complete NSCAT data set. The NSCAT and NASA Team signatures are very similar. For both, the melt cycle along with a portion of the freeze cycle is evident. These results are similar in form to those of *Gloersen*

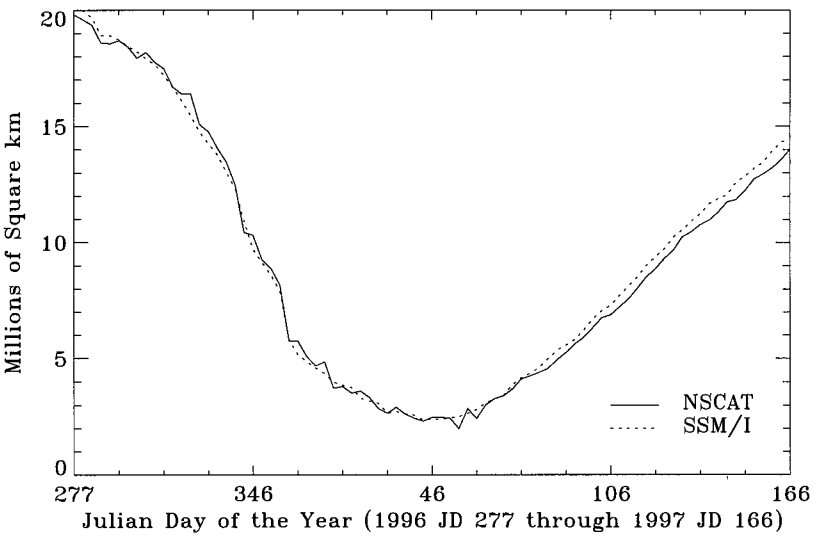

Figure 10. Seasonal Antarctic sea-ice extent in square kilometers using both the NSCAT and NASA Team methods. The data set extends from 1996 JD 277–282 to 1997 JD 166–171. The first Julian day of each imaging period is represented on the horizontal axis.

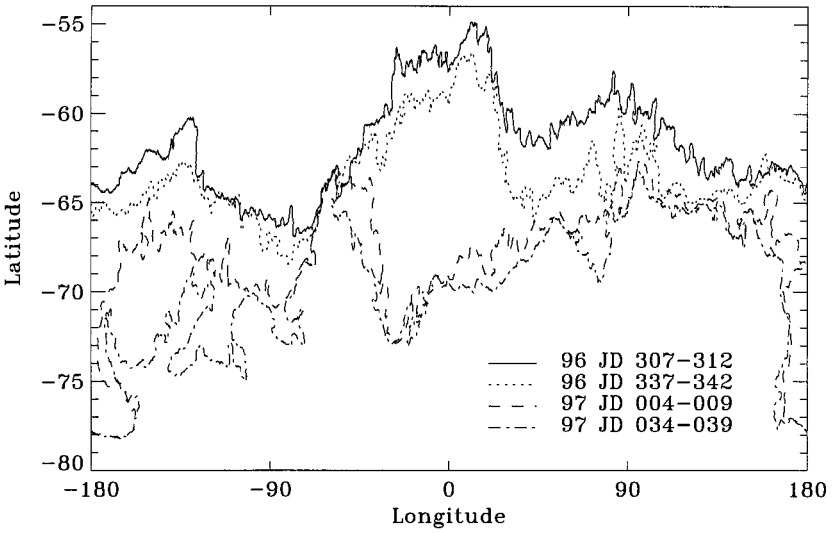

Figure 11. Latitude of the sea-ice edge as a function of longitude for four sample images illustrating yearly melt. The edges were generated using the NSCAT ice extent mapping technique.

et al. [1992] who computed the ice extent using the scanning multichannel microwave Radiometer (SMMR) from 1978 to 1987, although the maximum and minimum of the cycle are more extreme in 1996–1997.

We note that during the ice retreat phase, NSCAT often estimates a greater ice extent than the NASA Team algorithm. This result is similar to the findings of *Fetterer et al*. [1992] during midsummer, in which the Geosat altimeter measured a greater ice extent than the NASA Team SSM/I derived product. During ice advance the NASA Team method consistently predicts a larger sea-ice extent than NSCAT. The differences occur primarily in the Weddell and Amundsen Seas. The geographical correlation suggests that a geophysical cause is responsible for the discrepancy. Both of these areas are regions of rapid ice advance. The physical mechanisms behind these differences are presently not understood but may be related to differences in the detection of new ice formation for active and passive sensors similar to the differences noted by Fetterer et al. during ice retreat. The evolution of the sea-ice extent is shown in Figure 11. The latitude of the four sample ice edges is plotted as a function of longitude, illustrating the recession of the ice edge from October to February.

The ice extent mapping technique can also be applied to Arctic NSCAT data. Figure 12 shows an example Arctic SIRF A_v ice-masked images for 1997 JD 4–9, with the associated NASA Team edge plotted over it. Again, the resulting ice edge is similar to the NASA Team algorithm SSM/I derived edge.

5. Discussion

NSCAT dual-polarization Ku band data in concert with the SIRF resolution enhancement algorithm can be used to effectively determine sea-ice extent in the polar regions. The copol ratio and the incidence angle dependence of σ^o are used as primary classification parameters since they appear to be the most sensitive to the presence of sea ice. The κ parameter, on the other hand, is useful for correcting errors in the linear and quadratic ice extent estimates owing to its sensitivity to classification error inducing high winds in ocean regions. The technique requires no a priori information and adapts to the temporal variability of the underlying parameter distributions. When applied, the sea-ice detection method closely matches the NASA Team algorithm SSM/I derived 30% ice concentration extent. While we have used only scatterometer data to estimate the sea-ice extent, we believe that scatterometer data can be coupled with radiometer data to improve the accuracy of ice maps and ice classifications.

Application of the described technique has resulted in a large data set composed of 6-day average ice extent images every 3 days of the polar regions during the 9-month NSCAT mission. This data set can be applied to a wide range of studies, including global climate studies and wind processing. By excluding regions with ice cover, the probability of error in extracting wind speed and direction from the backscatter data goes down.

The loss of the ADEOS satellite prematurely terminated the flow of NSCAT data. While the ice-mapping technique was developed to be used with NSCAT data, it can be extended to work for future Ku band scatterometers with only minor changes. Two future scatterometers are of interest: QUIKSCAT will be launched in late 1998 and SeaWinds in 2000. These differ from NSCAT in several ways. First, they are dual-polarization, scanning pencil beam scatterometers. The inner scan is at 47° incidence and is horizontally polarized [$A_h(47)$], while the outer scan operates at 55° and is vertically polarized [$A_v(55)$] [*Spencer et al*., 1997]. Hence they do not contain the information needed to obtain an estimate of σ^o incidence angle dependence. Also, since the vertical and horizontal σ^o data are at different incidence angles, the copol ratio is undefined for QUIKSCAT and SeaWinds. However, by using two different primary classification parameters, A_h and $A_v(55)/A_h(47)$, the ice-mapping technique can still be applied. We found that using simulated SeaWinds data, the sea ice can still be mapped although the occurrence of error went up slightly.

An advantage of the QUIKSCAT and SeaWinds instruments over NSCAT is the increased coverage of the Earth's surface. Both have a wider swath than NSCAT and have no nadir gap, allowing QUIKSCAT and SeaWinds polar images

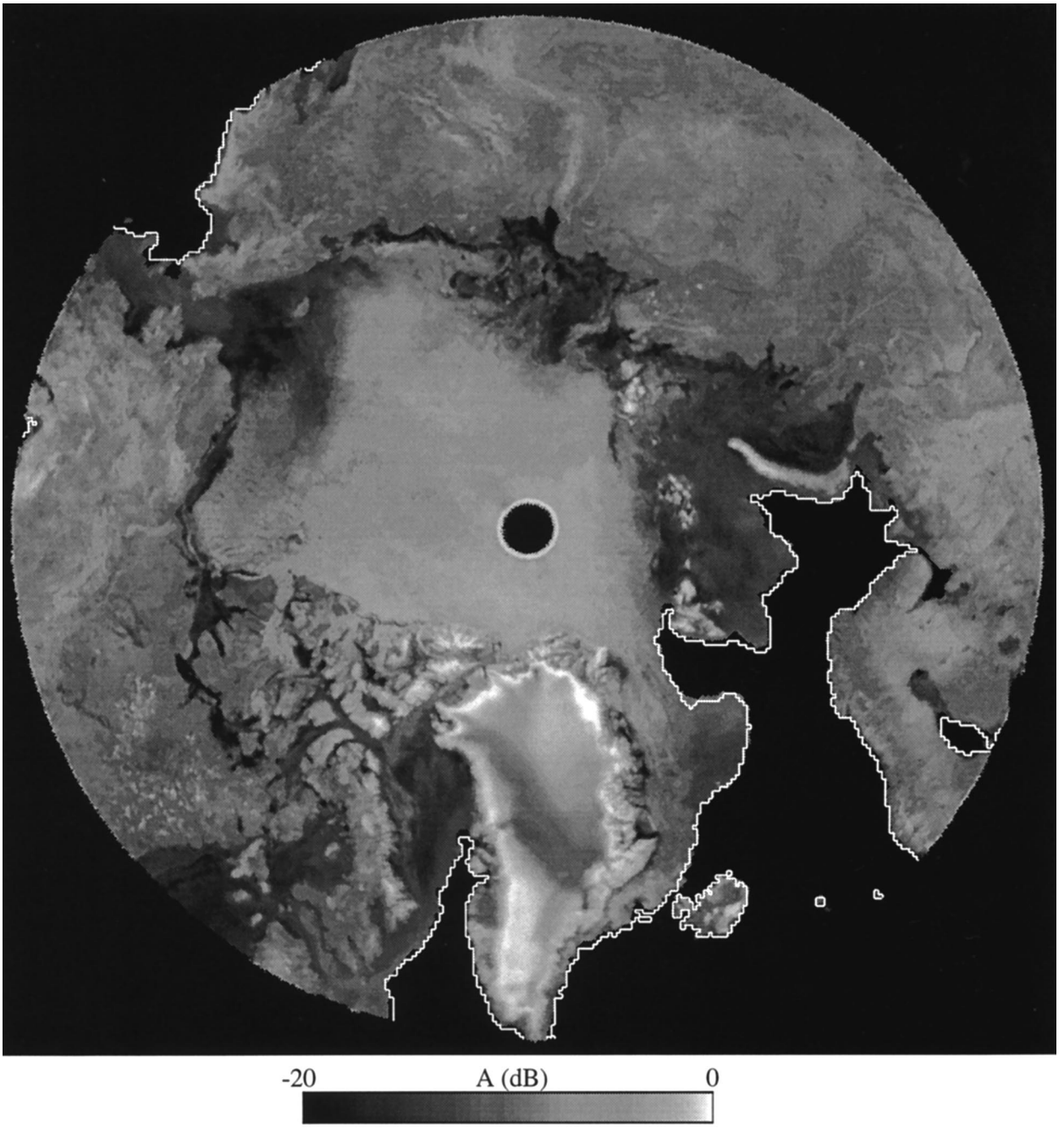

Figure 12. Arctic ice-masked image using the NSCAT technique for 1997 JD 4–9. The SSM/I derived ice edge is plotted in white over the top of this image for comparison.

to be produced using only 1–2 days of data rather than the 6 days required for NSCAT. As a result, the ice extent maps can be produced at 1- to 2-day intervals with quality and resolution similar to the NSCAT 6-day ice extent estimates. In this case, sea ice dynamics become less of a factor in discrimination errors near the edge. Alternatively, 6 days of QUIKSCAT or SeaWinds data can be used, resulting in a higher confidence ice extent map owing to the increased quality of parameter estimates.

Acknowledgments. This work was completed at the Brigham Young University Microwave Earth Remote Sensing Laboratory and was supported by the National Aeronautic and Space Administration. NSCAT data were obtained from the PO.DAAC at the Jet Propulsion Laboratory, Pasadena, California. SSM/I ice concentration data were obtained from the EOS DAAC at the National Snow and Ice Data Center, University of Colorado, Boulder. We thank Mark Drinkwater for his helpful comments and James Dyal for his help with the image processing.

References

Budd, W. F., Antarctic sea ice variations from satellite sensing in relation to climate, *IEEE Trans. Geosci. Remote Sens*., 15, 417–426, 1975.

Cavalieri, D. J., P. Gloersen, and W. J. Campbell, Determination of sea ice parameters with the Nimbus-7 SMMR, *J. Geophys. Res*., *89*(D4), 5355–5369, 1984.

Cavalieri, D. J., J. P. Crawford, M. R. Drinkwater, D. T. Eppler, L. D.

Farmer, R. R. Jentz, and E. C. Wackerman, Aircraft active and passive microwave validation of sea ice concentration from the Defense Meteorological Satellite Program Special Sensor Microwave Imager, *J. Geophys. Res*., *96*(C12), 21,989–22,008, 1991.

Drinkwater, M. R., Active microwave remote sensing observations of Weddell Sea ice, in *Antarctic Sea Ice: Physical Processes, Interactions and Variability*, *Antarct. Res. Ser*., vol. 74, edited by M. O. Jeffries, pp. 173–186, AGU, Washington, D.C., 1998.

Duda, R. O., and P. E. Hart, *Pattern Classification and Scene Analysis*, 482 pp., John Wiley, New York, 1973.

Early, D. S., and D. G. Long, Azimuthal modulation of C-band scatterometer σ^o over Southern Ocean sea ice, *IEEE Trans. Geosci. Remote Sens*., *35*, 1201–1209, 1997.

Fetterer, F. M., M. R. Drinkwater, K. C. Jezek, S. W. C. Laxon, R. G. Onstott, and L. M. H. Ulander, Sea ice altimetry, in *Microwave Remote Sensing of Sea Ice*, *Geophys. Monogr. Ser*., vol. 68, edited by F. D. Carsey, pp. 111–135, AGU, Washington, D. C., 1992.

Gloersen, P., W. J. Campbell, D. J. Cavalieri, J. C. Comiso, C. L. Parkinson, and H. J. Zwally, *Arctic and Antarctic Sea Ice, 1978–1987: Satellite Passive-Microwave Observations and Analysis*, 290 pp., Sci. and Tech. Inf. Program, ASA, Washington, D. C., 1992.

Gohin, F., Some active and passive microwave signatures of Antarctic sea ice from mid-winter to spring 1991, *Int. J. Remote Sens*., *16*(11), 2031–2054, 1995.

Gohin, F., and A. Cavanie, A first try at identification of sea ice using the three beam scatterometer of ERS-1, *Int. J. Remote Sens*., *15*(6), 1221–1228, 1994.

Hosseinmostafa, A. R., V. I. Lytle, K. C. Jezek, S. P. Gogineni, S. F. Ackley, and R. K. Moore, Comparison of radar backscatter from Antarctic and Arctic sea ice, *J. Electromagn. Waves Appl*., *9*(3), 421–438, 1995.

Long, D. G., and M. Drinkwater, Greenland Ice-Sheet surface properties observed by the Seasat-A Scatterometer at enhanced resolution, *J. Glaciol*., *40*(135), 213–230, 1994.

Long, D. G., P. Hardin, and P. Whiting, Resolution enhancement of spaceborne scatterometer data, *IEEE Trans. Geosci. Remote Sens*., *31*, 700–715, 1993.

Naderi, F. M., M. H. Freilich, and D. G. Long, Spaceborne radar measurement of wind velocity over the ocean—An overview of the NSCAT Scatterometer system, *Proc. IEEE*, *79*(6), 850–866, 1991.

Remund, Q. P., D. S. Early, and D. G. Long, Azimuthal modulation of Ku-band scatterometer σ^o over the Antarctic, *MERS Tech. Rep. 97-02*, 24 pp., Microwave Earth Remote Sens. Lab., Brigham Young Univ., Provo, Utah, 1997.

Rouse, J. W., Arctic ice type identification by radar, *Proc. IEEE*, *57*, 605–611, 1969.

Rush, J. C., *The Image Processing Handbook*, 2nd ed., 674 pp., CRC Press, Boca Raton, Fla., 1995.

Spencer, M. W., C. Wu, and D. G. Long, Tradeoffs in the design of a spaceborne scanning pencil beam scatterometer: Applications to SeaWinds, *IEEE Trans. Geosci. Remote Sens*., *35*, 115–126, 1997.

Yueh, S. H., R. Kwok, S. Lou, and W. Tsai, Sea ice identification using dual-polarized Ku-band scatterometer data, *IEEE Trans. Geosci. Remote Sens*., *35*, 560–569, 1997.

D. G. Long and Q. P. Remund, Department of Electrical and Computer Engineering, Brigham Young University, Provo, UT 84604. (e-mail: long@ee.byu.edu; remundq@ee.byu.edu)

(Received February 25, 1998; revised July 8, 1998;
accepted July 14, 1998.)